

Dispersive MHD turbulence in one dimension

D. Laveder, L. Marradi, T. Passot, P.L. Sulem

*Université de Nice Sophia Antipolis, CNRS, Observatoire de la Côte d'Azur,
BP 4229, 06304 Nice Cedex 4, France*

Abstract

Numerical simulations of dispersive turbulence in magnetized plasmas based on the Hall-MHD description are presented, assuming spatial variations along a unique direction making a prescribed angle with the ambient magnetic field. Main observations concern the energy transfers among the different scales and the various types of MHD waves, together with the conditions for the establishment of pressure-balanced structures. For parallel propagation, Alfvén-wave transfer to small scales is strongly inhibited and rather feeds magnetosonic modes, unless the effect of dispersion is strong enough at the energy injection scale. In oblique directions, the dominantly compressible character of the turbulence is pointed out with, for quasi-transverse propagation, the presence of conspicuous kinetic Alfvén waves. Preliminary simulations of a Landau fluid model incorporating relevant linear kinetic effects reveal the development of a significant plasma temperature anisotropy leading to recurrent instabilities.

Keywords: dispersive waves, Hall-MHD, turbulence

PACS: 52.65.Kj, 52.35.Bj

1. Introduction

Turbulence in magnetized plasmas remains a main issue in the understanding of the dynamics of media such as the solar corona, the interstellar medium, the solar wind or the planet magnetosheaths. In the solar wind for example the turbulent cascade extends much beyond the ion Larmor radius. One of the questions concerns the spectrum of the magnetic fluctuations that displays a power-law behavior on a broad range of wavenumbers, with a conspicuous change of slope near the inverse ion gyroradius (Leamon et al., 1998; Golstein and Roberts, 1999; Alexandrova et al., 2006; Sahraoui et al., 2009). This effect is often associated with the influence of wave dispersion, induced by the Hall current (Ghosh et al., 1996; Galtier, 2006; Alexandrova et al., 2007; Galtier and Buchlin, 2007; Servidio et al., 2007; Shaikh and Shukla, 2009), but could also result from a superposition of cascades of kinetic Alfvén waves and ion entropy fluctuations, as suggested by studies based on the gyrokinetic formalism (Howes et al., 2008b,a; Schekochihin et al., 2009).

At scales large compared with the ion inertial length or the ion Larmor radius, the usual MHD description provides a satisfactory description of regimes where, due to the presence of a strong ambient field, a dominant effect is the anisotropic energy transfer to Fourier modes with large

transverse wavenumbers (see e.g. Ghosh and Golstein (1997); Oughton and Matthaeus (2005) and references therein). This suggests that the dynamics of transverse small scales may be amenable to a reduced MHD description ((Zank and Matthaeus, 1992) and references therein), possibly including Hall current (Gómez et al., 2008) or, when retaining scales significantly smaller than the ion Larmor radius, to a gyrokinetic approach (Howes et al., 2006; Schekochihin et al., 2009). The latter that appears to be very efficient in describing strongly-magnetized near-equilibrium fusion plasmas is still under discussion concerning its applicability to space and astrophysical plasmas (Matthaeus et al., 2008). In the solar wind for example magnetic fluctuations may be comparable to the ambient field. Furthermore, longitudinal transfer could a priori be non negligible in a compressible regime, at scales where Hall current and kinetic effects play a significant role. A weak turbulence theory performed on the Vlasov-Maxwell system was recently developed (Yoon and Fang, 2008), showing the existence of a parallel cascade of low-frequency Alfvén waves through a three-wave decay process mediated by ion-sound turbulence, in a regime where wave-particle interactions are neglected. Addressing this issue by direct numerical simulations of the Vlasov-Maxwell equations being still difficult on the present-day computers, the question arises whether a similar cascade can be observed within a fluid model that retains important ingredients of the above theory, such as compressibility and dispersion. As a first step, we address the problem within the simplest description provided by Hall-MHD (HMHD) with Ohmic and viscous dissipations, together with a large-scale

Email addresses: laveder@oca.eu (D. Laveder),
marradi@oca.eu (L. Marradi), passot@oca.eu (T. Passot),
sulem@oca.eu (P.L. Sulem)

external driving acting on the transverse components of the velocity or magnetic field. We specifically concentrate on a one-dimensional setting where the variations of the fields are restricted to a direction making a prescribed angle with the ambient magnetic field, a framework that already reveals a manifold of complex dynamical processes that deserve detailed investigations before including additional physical and multidimensional effects. In the case of quasi-transverse propagation, we also present simulations of a model that extends the HMHD by retaining pressure anisotropy, Landau damping and finite Larmor radius effects up to transverse scales significantly smaller than the ion Larmor radius. This approach developed in Passot and Sulem (2007) extends the so-called Landau fluid model initiated in Snyder et al. (1997) for the MHD scales where Landau damping is the only relevant kinetic effect.

The paper is organized as follows. Section 2 briefly reviews the Hall-MHD description and its one-dimensional reduction. Section 3 concentrates on the case where the dynamics takes place in the direction of the ambient field. The case of oblique propagation is addressed in Section 4. Landau fluid simulations retaining small-scale kinetic effects are reported in Section 5. Our conclusions are summarized in Section 6.

2. The Hall-MHD description

HMHD can be viewed as a bi-fluid description of a plasma, where electron inertia is neglected. The presence of the Hall term in the generalized Ohm's law allows a decoupling of the ion fluid from the electron one in which the magnetic field lines are frozen. The validity conditions of HMHD are discussed in Howes (2009) where comparisons with kinetic theory are presented. Choosing as units the Alfvén speed, the amplitude of the ambient magnetic field, the equilibrium density and the ion inertial length l_i (defined as the ratio of the Alfvén speed to the ion gyrofrequency), the HMHD equations (for the ion fluid) read

$$\partial_t \rho + \nabla \cdot (\rho \mathbf{v}) = 0 \quad (1)$$

$$\rho(\partial_t \mathbf{v} + \mathbf{v} \cdot \nabla \mathbf{v}) = -\frac{\beta}{\gamma} \nabla \rho^\gamma + (\nabla \times \mathbf{b}) \times \mathbf{b} \quad (2)$$

$$\partial_t \mathbf{b} - \nabla \times (\mathbf{v} \times \mathbf{b}) = -\nabla \times \left(\frac{1}{\rho} (\nabla \times \mathbf{b}) \times \mathbf{b} \right) \quad (3)$$

$$\nabla \cdot \mathbf{b} = 0, \quad (4)$$

where the total β parameter is the square ratio of the sound to Alfvén velocities, and a polytropic equation of state $p \propto \rho^\gamma$ is assumed for both ions and electrons.

When the spatial variation is restricted to a dependency on the x coordinate along a direction making an angle θ with the ambient magnetic field $\mathbf{B}_0 = (\cos \theta, \sin \theta, 0)$, one gets

$$\partial_t \rho + \partial_x (\rho v_x) = 0 \quad (5)$$

$$\partial_t v_x + v_x \partial_x v_x = -\frac{1}{\rho} \partial_x \left(\frac{\beta}{\gamma} \rho^\gamma + \frac{1}{2} (b_y^2 + b_z^2) \right)$$

$$+ \frac{\mu_x}{\rho} \partial_{xx} v_x \quad (6)$$

$$\partial_t v_{[y,z]} + v_x \partial_x v_{[y,z]} = \frac{\cos \theta}{\rho} \partial_x b_{[y,z]} + \frac{\mu_{[y,z]}}{\rho} \partial_{xx} v_{[y,z]} + f_{[y,z]}^v \quad (7)$$

$$\partial_t b_{[y,z]} - b_x \partial_x v_{[y,z]} + \partial_x (v_x b_{[y,z]}) = \pm \cos \theta \partial_x \left(\frac{1}{\rho} \partial_x b_{[y,z]} \right) + \kappa_{[y,z]} \partial_{xx} b_{[y,z]} + f_{[y,z]}^b \quad (8)$$

where driving and dissipation have been supplemented in both the velocity and magnetic field equations. Here, the subscript $[y, z]$ refers to the vector component along the y or the z direction, or to the value of the viscosity acting on the corresponding velocity component. The \pm sign in front of the Hall term depends on the considered component of the magnetic field. No (artificial) hyperviscosity and magnetic diffusivity nor spectral filtering are used in the simulations. Instead, anisotropic dissipations are assumed. In the case of parallel propagation, different viscosities and diffusivities are taken in the directions parallel and transverse to the ambient field, by prescribing $\kappa_y = \kappa_z = \mu_y = \mu_z \ll \mu_x$. For oblique propagation, we assume smaller coefficients in the direction perpendicular to the plane defined by the magnetic field and the direction of propagation, in the form $\kappa_z = \mu_z \ll \mu_x = \mu_y = \kappa_y$.

The driving is assumed to act either on the velocity (kinetic driving) or the magnetic field (magnetic driving) components. For parallel propagation, we prescribe $f_y^v = f_z^v$ or $f_y^b = f_z^b$ while, for oblique propagation, the driving reduces to f_z^v or to f_z^b . Such a driving is supposed to minimize the sonic components, as it is acting on field components perpendicular to the ambient field in parallel propagation and to the plane defined by the ambient field and the propagation direction when the latter is oblique. The values of the diffusivity and viscosities in the various directions are chosen as the minimal values (depending on the spatial resolution and of the physical parameters of the runs) needed to accurately resolve all the retained scales.

In all the simulations, we take $\gamma = 5/3$ and $\beta = 2$. Each component of the kinetic or magnetic driving (generically denoted f) is a white noise in time defined by its Fourier transform $\hat{f}_k = C \xi \sqrt{F_k / \Delta t}$ where ξ is a Gaussian random variable with zero mean and unit variance, chosen independently at each time step. This ensures a constant mean flux of energy injection that can be chosen at will, as in the usual phenomenology of the turbulent cascades. Furthermore, such a driving process avoids an artificial enhancement of a specific type of waves and enables the emergence of the dominant modes as the result of the nonlinear dynamics. The spectral distribution $F_k = k^4 \exp(-(2k^2/k_f^2))$ is peaked about a wavenumber k_f .

The HMHD system is integrated in a periodic domain using a Fourier pseudo-spectral method where most of the aliasing is removed by spectral truncation of the computed nonlinear terms at $2/3$ of the maximal wavenumber. The spatial resolutions given in the following sections are the

effective ones, after aliasing has been suppressed. In all the simulations, the temporal scheme is a third-order low-storage Runge-Kutta (Williamson, 1980). Resolving all the temporal scales present in the system, this scheme accurately preserves the dispersion relation of all the linear modes retained in the simulation, in contrast with implicit or semi-implicit schemes (Laveder et al., 2009).

For convenience, we collected in Table 1, the main parameters characterizing the simulations discussed in the forthcoming sections.

As seen in the following, in spite of the turbulent regime achieved in the HMHD simulations discussed in this paper, signatures of the linear waves are often present. It is thus useful to briefly review the linear theory of eigenmodes for the HMHD equations in the absence of dissipation and driving. By linearizing eqs. (5)-(8) about the equilibrium state associated to $\rho = 1$, $b_x = \cos \theta$, $b_y = \sin \theta$, one derives that the (real) eigenfrequencies ω_i with $i = 1, 2, 3$ obey the dispersion relation

$$\omega^6 - k^2(1 + \beta + \cos^2 \theta + k^2 \cos^2 \theta)\omega^4 + k^4 \cos^2 \theta(2\beta + 1 + \beta k^2)\omega^2 - \beta k^6 \cos^4 \theta = 0, \quad (9)$$

where it is sufficient to concentrate on the positive solutions.

Assuming an oblique propagation, the corresponding eigenmodes are given by

$$\mathbf{W}^{(i)} = (\rho, v_x = \alpha_{v_x}^{(i)} \rho, v_y = \alpha_{v_y}^{(i)} \rho, v_z = \alpha_{v_z}^{(i)} \rho, b_y = \alpha_{b_y}^{(i)} \rho, b_z = \alpha_{b_z}^{(i)} \rho) \quad (10)$$

with

$$\alpha_{v_x}^{(i)} = \frac{\omega_i}{k} \quad (11)$$

$$\alpha_{b_y}^{(i)} = \frac{(k^2 \cos^2 \theta - \omega_i^2) \sin \theta}{k^4 \cos^2 \theta - \left(\frac{k^2}{\omega_i} \cos^2 \theta - \omega_i\right)^2} \quad (12)$$

$$\alpha_{b_z}^{(i)} = \frac{-ik^2 \omega_i \sin \theta \cos \theta}{k^4 \cos^2 \theta - \left(\frac{k^2}{\omega_i} \cos^2 \theta - \omega_i\right)^2} \quad (13)$$

$$\alpha_{v_y}^{(i)} = -\cos \theta \frac{k}{\omega_i} \alpha_{b_y}^{(i)} \quad (14)$$

$$\alpha_{v_z}^{(i)} = -\cos \theta \frac{k}{\omega_i} \alpha_{b_z}^{(i)}. \quad (15)$$

The variation of these coefficients with the wavenumber k is displayed in fig. 1 for $\theta = 45^\circ$ and $\theta = 80^\circ$.

For parallel propagation ($\theta = 0$), the sonic wave for which $\omega = \sqrt{\beta}k$ decouples from the eigenmodes corresponding to (circularly-polarized) Alfvén waves. The latter obey $b_y + ib_z = -(\omega/k)(v_y + iv_z) \propto \exp[i\sigma(kx - \omega t)]$ where $\sigma = -1$ or 1 , depending of the left-hand (LH) or right-hand (RH) polarization, with the dispersion relation $\omega_\sigma = (\sigma/2)k^2 + k(1 + k^2/4)^{1/2}$. In the large wavenumber limit, the frequency of LH polarized waves saturates, while it grows like k^2 in the case of RH polarization. At frequencies beyond the HMHD asymptotics, the RH polarized Alfvén waves are continued into whistler waves, while

the LH polarized waves become ion-cyclotron waves. It is noticeable that the dispersive parallel Alfvén waves are also exact solutions of the nonlinear HMHD problem.

For an oblique direction of propagation and $\beta > 1$, we still refer to the eigenmode corresponding to the smallest eigenvalue ω_1 , that is dominated by the field components v_y, v_z (fig. 1), as the ion-cyclotron wave. In the case of quasi-transverse propagation, it is often called the kinetic Alfvén wave. The intermediate mode corresponding to the eigenvalue ω_2 is the one that reduces to a pure sonic mode for $\theta = 0$. For oblique propagation it is dominated by the v_x component at small scales only, while at large scales b_z and v_z prevail. The mode at highest frequency ω_3 , which corresponds to the whistler wave for $\theta = 0$, has properties opposite to those of the intermediate one. For oblique propagation, it is usually viewed as a whistler wave at small scales only (Krauss-Varban et al., 1994). For the sake of simplicity, we will keep this terminology at large scales also, where this mode is strongly compressible.

3. Parallel dynamics

3.1. Large-scale driving

We first consider a domain of extension $L = 16\pi$ in a direction parallel to the ambient magnetic field. We use a transverse kinetic or a magnetic driving characterized by the parameters $C = 0.1$ and $k_f = 0.5$ corresponding to a mode index $n_f = 4$. Defining the ion inertial wavenumber as $k_i = 2\pi/l_i$, this corresponds to a ratio $k_i/k_f = 4\pi$. A spatial resolution of 1024 grid points is used, which prescribes a time step as small as $\Delta t = 5 \cdot 10^{-5}$, due to the dispersion relation of the whistler modes. We use a viscosity $\mu_x = 10^{-1}$ in the equation for the parallel velocity, and equal viscosity and magnetic diffusivity $\mu_y = \mu_z = \kappa_y = \kappa_z = 10^{-6}$ for the transverse fields. This relatively large viscosity in the parallel direction is required because of the development of shock waves.

In the case of kinetic driving (run A), fig. 2 (left) shows the time evolution of the total energy of the system (from which the initial value has been subtracted) $E = \int (\frac{\rho}{2}|\mathbf{v}|^2 + \frac{1}{2}(|\mathbf{b}|^2 - 1) + \frac{\beta}{\gamma(\gamma-1)}(\rho^\gamma - 1))dx$. It also displays the contributions of the transverse kinetic $E_\perp^V = \int \frac{\rho}{2}|\mathbf{v}_\perp|^2 dx$ and magnetic $E_\perp^M = \int \frac{1}{2}|\mathbf{b}_\perp|^2 dx$ energies that turn out to be comparable and much larger than the parallel kinetic and the internal energies (not shown). It is conspicuous that the energy does not saturate, even after an integration time $t = 20000$. Figure 2 (right) displays the time evolution of the magnetic energy on the modes of index 1, 2, 3, 4 (a similar behavior is obtained for the kinetic modes). We observe that after a while, the mode of index $n = 1$ becomes strongly dominant, indicating a significant inverse transfer to larger and larger scales (leading to a non saturation of the energy), as expected from an equilibrium thermodynamical argument (Servidio et al., 2008), up to the moment when it reaches the size of the computational domain.

run	domain size	propagation angle	driving
A	$L = 16\pi$	$\theta = 0^\circ$	kinetic, $C = 0.1$, $k_f l_i = 1/2$
B	$L = 16\pi$	$\theta = 0^\circ$	magnetic, $C = 0.1$, $k_f l_i = 1/2$
C	$L = 4\pi$	$\theta = 0^\circ$	kinetic, $C = 6.25 \times 10^{-3}$, $k_f l_i = 2$
D	$L = 4\pi$	$\theta = 0^\circ$	magnetic, $C = 6.25 \times 10^{-3}$, $k_f l_i = 2$
E	$L = 16\pi$	$\theta = 45^\circ$	kinetic, $C = 0.1$, $k_f l_i = 1/2$
F	$L = 4\pi$	$\theta = 45^\circ$	kinetic, $C = 6.25 \times 10^{-3}$, $k_f l_i = 2$
G	$L = 4\pi$	$\theta = 45^\circ$	magnetic, $C = 6.25 \times 10^{-3}$, $k_f l_i = 2$
H	$L = 16\pi$	$\theta = 80^\circ$	kinetic, $C = 0.1$, $k_f l_i = 1/2$

Table 1: Simulation parameters of HMHD simulations

A main observation is the establishment of a pressure-balanced state (fig. 3, left) that is not limited to the largest scales, in the sense that pressure balance is still observed when the largest Fourier modes are filtered out. Inspection of the square transverse velocity $|\mathbf{v}_\perp|^2$ (fig. 3, right) shows the presence of small scales superimposed to the $n = 1$ mode, which are more conspicuous than on the magnetic component $|\mathbf{b}_\perp|^2$ displayed on the left panel. When filtering out the modes of index $n = 1$, the square transverse velocity $|\mathbf{v}_\perp|^2$ reveals the presence of solitonic waves which in many instances survive collisions and preserve their coherence on several time units (fig. 4, left). It is of interest to notice that dispersive pressure-balanced structures are commonly observed in space plasmas (see e.g. (Stasiewicz et al., 2003)). The right panel that displays the individual transverse velocity components also shows the presence of rotational discontinuities (near $x = 4\pi$), together with the existence of fluctuations at very small scales.

Figure 5 displays the transverse kinetic $|\hat{\mathbf{v}}_y|^2 + |\hat{\mathbf{v}}_z|^2$ (thick line) and magnetic $|\hat{\mathbf{b}}_y|^2 + |\hat{\mathbf{b}}_z|^2$ (thin line) spectra, averaged over the time intervals $t = 18200 - 18250$ (left), and $t = 19500 - 19550$ (right). The left panel corresponds to a stage of the evolution for which fig. 4 provides instantaneous snapshots. We can distinguish various spectral ranges, and in particular two different power-law domains at large and intermediate scales whose exponents fluctuate in time while preserving a kinetic spectrum shallower than the magnetic one. Such a dominance of the kinetic on the magnetic contribution suggests an ion-cyclotron turbulence since for these waves the transverse velocity and magnetic field components are in a ratio $k/\omega > 1$. The transition between the two spectral ranges occurs near $k \approx k_i = 2\pi$ (reminiscent of observations in the solar wind and magnetosheath (Leamon et al., 1998; Golstein and Roberts, 1999; Alexandrova et al., 2006; Sahraoui et al., 2009)) that corresponds to the typical scale of the solitonic structures seen in fig. 4. The flat region visible at larger wavenumbers is the spectral signature of the small-scale fluctuations visible in physical space. At longer times (right panel), the intermediate power-law range has extended as the soliton amplitude increased, taking over the flat spectral region.

In the case of a magnetic driving (run B), a similar overall dynamics is obtained but on a longer time scales (not shown). The energy accumulation on the largest scale is slower by a factor four to five, and the pressure balance is less conspicuous even at the end of the simulation ($t = 10000$). Furthermore, no clear power law spectra have developed.

Further insight on the dynamics is provided by the dissipation of the various fields. Figure 6 (left) displays the time evolution (averaged over a time interval of 1000 time units) of the viscous dissipation $D_\parallel = \int \mu_x (\partial_x v_x)^2 dx$ originating from the parallel velocity for the two types of driving. The dissipation observed is slightly larger in the case of magnetic driving and reflects a stronger direct energy transfer to sonic waves. This observation is consistent with the better pressure balance obtained with kinetic than with magnetic forcing. On the right panel is displayed the (similarly averaged) dissipation $D_\perp = \int (\mu_y (\partial_x v_y)^2 + \mu_z (\partial_x v_z)^2 + \kappa_y (\partial_x b_y)^2 + \kappa_z (\partial_x b_z)^2) dx$ of the transverse fields, that turns out to be larger in the case of kinetic driving, indicating a more efficient transfer to small scales for the transverse fields.

Energy dissipation affects dominantly the parallel velocity component, the transverse dissipation being about two orders of magnitude smaller. This suggests that the injected energy is mainly transferred to sonic waves and dissipated through a cascade of acoustic waves. For parallel propagation, writing the equations for the energy density of the Alfvén and acoustic waves in the form ($\mu_\perp \equiv \mu_y = \mu_z$, $\kappa_\perp \equiv \kappa_y = \kappa_z$)

$$\begin{aligned}
& \partial_t \left(\frac{\rho}{2} |\mathbf{v}_\perp|^2 + \frac{1}{2} |\mathbf{b}_\perp|^2 \right) \\
& + \partial_x \left(\frac{1}{2} \rho |\mathbf{v}_\perp|^2 v_x + \frac{1}{2} \rho |\mathbf{b}_\perp|^2 v_x - \mathbf{v}_\perp \cdot \mathbf{b}_\perp + h_x \right) = \\
& - \frac{1}{2} |b_\perp|^2 \partial_x v_x + \mu_\perp \mathbf{v}_\perp \cdot \partial_{xx} \mathbf{v}_\perp + \kappa_\perp \mathbf{b}_\perp \cdot \partial_{xx} \mathbf{b}_\perp \\
& + \mathbf{v}_\perp \cdot \mathbf{f}_\perp^v + \mathbf{b}_\perp \cdot \mathbf{f}_\perp^b
\end{aligned} \tag{16}$$

$$\begin{aligned}
& \partial_t \left(\frac{\beta}{\gamma(\gamma-1)} \rho^\gamma + \frac{\rho}{2} v_x^2 \right) \\
& + \partial_x \left(\frac{\beta}{\gamma-1} p + \frac{1}{2} \rho v_x^3 + \frac{1}{2} v_x |\mathbf{b}_\perp|^2 \right) \\
& = \frac{1}{2} |b_\perp|^2 \partial_x v_x + \mu_x v_x \partial_{xx} v_x + v_x f_x^v + b_x f_x^b
\end{aligned} \tag{17}$$

where

$$h_x = \frac{1}{\rho} \epsilon_{j1q} b_j b_x \partial_x b_q \quad (18)$$

arises from the Hall term, we get that the energy transfer from the Alfvén to sonic waves is given by

$$S = \frac{1}{2} \int |\mathbf{b}_\perp|^2 \partial_x v_x dx. \quad (19)$$

Figure 7 displays in the case of kinetic driving the time variation of S , together with that of the parallel (viscous) dissipation. Left panel, which corresponds to instantaneous quantities, shows that the amplitude fluctuations of the transfer are much larger than those of the dissipation. We nevertheless observe on the right panel which displays the same quantities averaged on a time interval of 1000 time units, that the parallel dissipation identifies in the mean with the energy transfer. A similar behavior is visible with the magnetic driving.

The above observations indicate that sonic wave turbulence is the dominant phenomenon, although small scales also form on the transverse field components on a longer time scale. In order to address more precisely the nature of the transfers, it is of interest to perform a simulation where the final time $t = 20000$ of the previous simulation is taken as initial condition and the energy is no longer injected at a constant rate, but the driving is monitored in order to maintain the total energy almost constant. This constraint leads to a drastic change on the transverse spectra which, within a few thousands of time units, loose energy at the scale of the solitons displayed in fig. 4, leading to a conspicuous spectral gap (fig. 8, left). In physical space, solitonic structures have indeed disappeared, the profile of $|\mathbf{v}_\perp|^2$ reducing to small-scale oscillations superimposed to large-scale quasi-sinusoidal structures, as seen in fig. 8 (right) where the strongly dominant mode $n = 1$ has been filtered out. At scales larger than the spectral gap, the pressure-balanced state persists, while at smaller scales viscous and Ohmic dissipations are negligible and dispersion is significant, thus permitting the small scales to persist. This suggests that, in the present simulation, the transfer of Alfvénic energy from large to intermediate Alfvén scales which in the previous simulation maintained the solitons, does not take place in the absence of a sufficiently strong driving, and thus cannot compensate the transfer of energy from the Alfvénic to the sonic modes at the soliton scales. The dynamics thus turns out to be significantly different from ordinary turbulence and should rather be viewed as a structure-dominated regime displaying significantly less universal properties.

A further characterization of the dynamics is provided by a frequency analysis on the spatial Fourier modes of the fields components. In contrast with the incompressible regime where the presence of the sole Alfvén waves makes convenient the analysis of time records at given points in physical space (Dmitruk and Matthaeus, 2009), the possible dominance of different modes at different scales in

the present case, leads to discriminate between different Fourier modes. Figure 9 displays the temporal spectrum of the spatial Fourier modes $k = 1$, $k = 4$ and $k = 25$ respectively, for the components v_x (blue), b_z (red) and v_z (green) for kinetic (run A: panels a,b,c) and magnetic (run B: panels d,e,f) driving. The analysis has been performed during a time interval close to the end of the simulations. At large scale ($k = 1 = 2k_f$), two peaks are visible. They correspond, up to a slight infrared shift possibly due to the presence of large-scale coherent structures, to the ion-cyclotron ($\omega \approx 0.62$) and the sonic ($\omega \approx 1.4$) frequencies. These peaks are wider with kinetic than with magnetic forcing, indicating stronger nonlinear couplings in the former case which is also characterized by a larger amount of transverse energy at all scales, with a ratio between the kinetic and magnetic components in qualitative agreement with the linear ion-cyclotron eigenmode. At smaller scales ($k = 25 \approx 4k_i$), the relative importance of the sonic peak decreases in the case of kinetic driving, but remains significant for magnetic driving, indicating a higher level of sonic turbulence in the latter regime.

3.2. Driving at smaller scales

In a second series of simulations, the global effect of the Hall term has been increased by injecting energy at smaller scales, with the aim to investigate the influence of dispersion on the energy transfers. To address this issue, the extension of the computational domain was reduced to $L = 4\pi$ and the system driven at $k_f = 2$, leading to a ratio $k_i/k_f = \pi$. The rate of energy injection was lowered by the same factor as the domain extension by taking $C = 6.25 \cdot 10^{-3}$, in order to preserve the same amount of energy injection per unit length. Reducing the resolution to 256 mesh points, ensures the same maximal wavenumber as in the simulations of Section 3.1. To preserve numerical stability, we had to use time steps $\Delta t = 3.125 \cdot 10^{-6}$ and $\Delta t = 2.5 \cdot 10^{-5}$ for the kinetic and magnetic drivings respectively. The required viscosities and magnetic diffusivities are now $\mu_x = 10^{-2}$, $\mu_y = \mu_z = \kappa_y = \kappa_z = 10^{-5}$ in both cases.

Kinetic (run C) and magnetic (run D) drivings lead now to significantly different dynamics. In the former case, the inverse cascade is less efficient than in the conditions of Section 3.1. The energy of the modes with $n = 1$ still increases up to the end of the simulation (not shown), but after a time of about 7000 times units, the accuracy of the simulation deteriorates, the temporal resolution becoming insufficient. The total energy grows slowly but in contrast with the conditions of Section 3.1, the transverse magnetic energy is now significantly lower than the kinetic one (fig. 10, left). Differently, in the case of a magnetic driving, kinetic and magnetic energies are comparable, and the system reaches a stationary steady state where the energies saturate (Fig. 10, right). In the case of a kinetic forcing, pressure-balanced structures are still present, while with a magnetic driving, no pressure balance establishes,

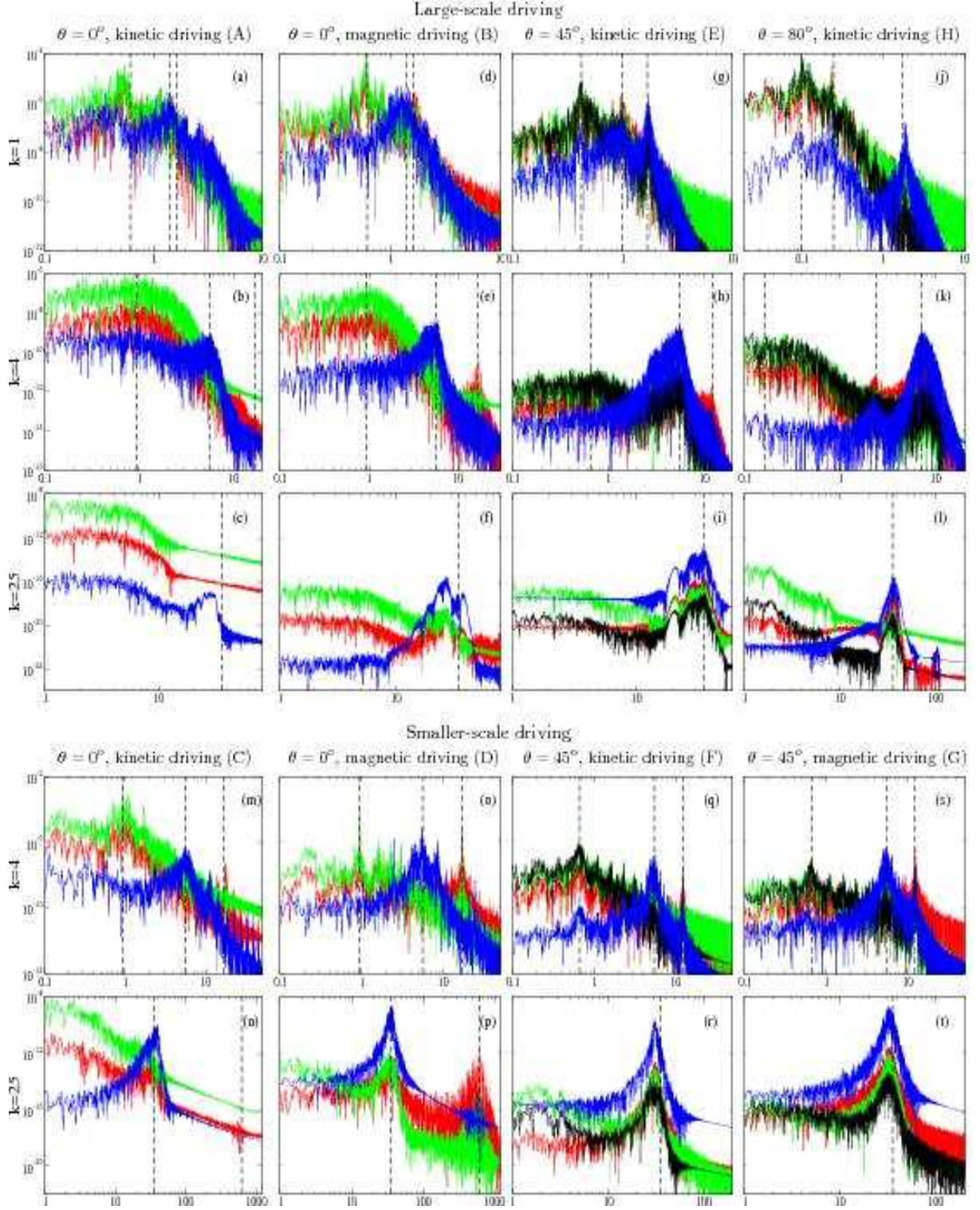


Figure 9: Frequency spectra $|\hat{b}_z|^2(k, \omega)$ (red), $|\hat{v}_z|^2(k, \omega)$ (green), $|\hat{v}_y|^2(k, \omega)$ (black), $|\hat{v}_x|^2(k, \omega)$ (blue) as functions of ω , at various wavenumbers k for the runs described in Sections 3 and 4 (see Table 1). The vertical lines refer to the three linear eigenfrequencies given by the dispersion relation (9). When only two lines are visible, they correspond to the two higher frequencies, while when only one is present, it is the intermediate one.

Figure 11 displays the profiles of $|\mathbf{v}_\perp|^2$ for kinetic (left panel) and magnetic (right panel) drivings, showing that more small scales develop in the former case. The structures are traveling much more slowly than with the large-scale forcing. Furthermore, when comparing transverse velocity and magnetic fields, we note that the latter is significantly smoother for both types of drivings.

The contrast between the two types of forcing is even more striking at the level of the dissipations (fig. 12). While for magnetic driving, dissipation is strongly dominant on the parallel magnetic field fluctuations, with the kinetic one it mostly affects the transverse components, indicating a reduced transfer to sonic waves and the possibility of a direct cascade of Alfvénic modes, in qualitative agreement with the weak-turbulence analysis performed by Yoon and Fang (2008) on the Vlasov equation. Furthermore, when the kinetic forcing is monitored in order to maintain a prescribed energy as in Section 3.1, no energy gap establishes, indicating that the structures can sustain a much more constant direct transfer than in the case of Section 3.1. This suggests the possibility of a more standard turbulence when the injection scale is sufficiently close to that at which structures form and dispersion acts efficiently.

The significant difference between the two forcings can be clarified by looking at the distribution of energy among the various modes and the different scales, presented in fig. 9. At large scale ($k = 4$, panel m), a peak is visible at the ion cyclotron frequency for both drivings, while whistler modes are also present in the case of magnetic driving (panel o). The relative intensity of the magnetic versus kinetic components is consistent with the properties of the corresponding eigenmodes. Note that with a magnetic driving, the peaks are especially sharp for the transverse modes. When the wavenumber is increased ($k = 25$), the peaks broaden under the effect of wave coupling. This leads to dominant ion cyclotron turbulence in the case of a kinetic forcing (panel n). With a magnetic driving (panel p), the sonic mode, visible on the left of the whistler peak at large scale, becomes dominant, while the whistler peak still remains conspicuous. To summarize, the pressure balance observed in the case of a kinetic driving is consistent with the small amplitude of the intermediate modes, while the transverse dynamics is dominated by ion-cyclotron modes that, with the present forcing, can cascade down to the dissipation scales. Differently, in the case of a magnetic driving, the transverse velocity is dominated by ion-cyclotron modes and the transverse magnetic field to whistler modes. The large amplitude of the latter waves prevents in particular the establishment of a pressure balance when the system is magnetically driven, which leads to an efficient generation of sonic modes that cascade and dissipate. In contrast, kinetic forcing does not drive whistler waves, so pressure balance can establish and sonic turbulence remains subdominant, leaving the possibility for a direct cascade of ion-cyclotron modes.

4. Oblique dynamics

As already mentioned, for oblique propagation, the system is driven on the z component of the velocity or the magnetic field, thus perpendicularly to the plane defined by the ambient field and the direction of propagation. The injection rate is the same as the injection on each component in the case of parallel propagation, and thus globally reduced by a factor two. Two typical angles are considered, $\theta = 45^\circ$ to exemplify a generic oblique regime, and $\theta = 80^\circ$ that corresponds to a quasi-transverse dynamics.

4.1. The case of 45° propagation angle

With a kinetic driving, the same computational domains and forcing scales as in Sections 3.1 and 3.2 were considered, while in the case of a magnetic driving, only the largest domain was considered. A resolution of 512 mesh points was used in all cases, with $\mu_x = \mu_y = \kappa_y = 2 \cdot 10^{-2}$, $\mu_z = \kappa_z = 10^{-6}$ and $\Delta t = 10^{-4}$ (large-scale forcing), $\mu_x = \mu_y = \kappa_y = 5 \cdot 10^{-3}$, $\mu_z = \kappa_z = 10^{-5}$ and $\Delta t = 5 \cdot 10^{-5}$ (smaller-scale forcing).

A main observation common to all these simulations is the absence of a significant energy transfer to the largest scales, but rather the establishment of a statistically steady state, with a total energy saturating at about the same level in all the runs, after about a thousand time units. In the case of the kinetic driving at large scales (run E), a pressure balance nevertheless establishes, perturbed by localized events associated with the formation of cusps on the longitudinal velocity profile (fig. 13). These peculiar structures are reminiscent of the intermediate shocks that develop in the Cohen-Kulsrud equation (Cohen and Kulsrud, 1974). The pressure balance deteriorates when the driving is at smaller scales, especially when it is of magnetic type.

At the level of the dissipations, the various types of driving do not induce qualitative differences. It is noticeable that the dissipation $D_z = \int (\mu_z (\partial_x v_z)^2 + \kappa_z (\partial_x b_z)^2) dx$ affecting the velocity and magnetic field components in the transverse direction is smaller by a factor of order 10^4 than the dissipation $D_{\text{plane}} = \int (\mu_x (\partial_x v_x)^2 + \mu_y (\partial_x v_y)^2 + \kappa_y (\partial_x b_y)^2) dx$ of the components in the (\mathbf{B}_0, \hat{x}) plane.

A more detailed understanding of the dynamics is provided by the frequency analysis displayed in fig. 9. With a large-scale kinetic forcing (run E: panels g, h, i), three distinct frequencies corresponding to the three linear eigenmodes with comparable amplitudes, are identified on the $k = 1$ mode. At smaller scales ($k = 4$ and $k = 25$), in contrast, a peak near the intermediate frequency is dominant and strongly broadened, with most of the energy contained in the component parallel to the direction of propagation, consistent with the properties of the corresponding eigenmodes displayed in fig. 1 (left). This confirms the compressible nature of the turbulence that develops at small scales.

When kinetic energy is injected at smaller scales (run F: panels q, r), the three eigenfrequencies are still visi-

ble at $k = 4$, with a much more intense contribution of the whistler modes when compared with the large-scale driving. The presence of whistler at large or intermediate scales which is even more conspicuous in the case of magnetic driving (run G: panels s, t), is expected to be at the origin of the disruption of the pressure balance, as also observed in the case of parallel propagation. At smaller scale ($k = 25$), the intermediate mode strongly dominates, as for the large-scale driving. In other words, in oblique directions the presence of dispersion makes the dynamics fully compressible, in contrast with parallel propagation where an incompressible Alfvénic turbulence can be isolated when concentrating on the transverse components of the fields.

4.2. The case of 80° propagation angle

In this case, the simulation was performed with a large-scale kinetic driving (run H), in the same conditions as in Section 4.1. A resolution of 512 mesh points was used, with $\mu_x = \mu_y = \kappa_y = 10^{-2}$, $\mu_z = \kappa_z = 10^{-6}$ and $\Delta t = 10^{-4}$. Compared with the 45° case, the energy saturates at a much later time ($t \approx 40000$). This long time interval is required because of the presence of an early inverse cascade that leads to a dominance of the $n = 1$ mode, which nevertheless saturates before the end of the simulation. A pressure-balanced state establishes very rapidly (fig. 14, left). It is nevertheless perturbed by dispersive shocks, which occur very frequently and are especially visible on the velocity component v_x , as displayed in fig. 14 (right) at $t = 2472$. The spectra of the transverse velocity and magnetic fields are displayed in fig. 15, averaged over the time intervals $t = 2465 - 2477$ (left) and $t = 10595 - 10565$ (right). Left panel represents a typical situation in which a dispersive shock is crossing the simulation box, its spectral signature being conspicuous as a flat zone at intermediate scales. Right panel represents instead the same spectra at a moment when no shocks are present. In such a case, the velocity spectrum is steeper than the magnetic one, in contrast with the case of parallel propagation where the opposite takes place. This is consistent with the domination of whistler modes at intermediate scales, as discussed below.

Inspection of fig. 9 (panels j, k, l) provides further insights on the dynamics. Compared with the 45° case (panels g, h, i), much more energy is contained at low frequency in all the spatial Fourier modes. The characteristics of the various field at large ($k = 1$) and intermediate ($k = 4$) scales where $v_y \approx v_z \gg v_x, b_y, b_z$, indicate that these modes can be viewed as ion-cyclotron waves (fig. 1), which for this angle of propagation identifies with the branch of kinetic Alfvén waves. At smaller scales ($k = 25$, panel l) $v_y \gg v_z$, probably because of the choice $\mu_y \gg \mu_z$. The oscillations in the dispersive shock displayed in fig. 14 (right) can be identified as the whistler modes associated with the broadened peak visible on the v_x field for $k = 4$ displayed in panel k. These high-frequency modes are indeed strongly dominated by the v_x component at these

scales, which is consistent with the properties of the linear whistler waves. As a consequence, they are not expected to significantly disrupt the pressure balance, in contrast with the 45° case with small-scale forcing. In the latter simulation, whistler modes are indeed present at scales where they involve a significant magnetic contribution. At $k = 4$, a weak peak corresponding to the intermediate frequency is also present. The corresponding mode dominates over the whistler wave at $k = 25$, where it reaches an amplitude comparable to the low-frequency components (panel l). The overall dynamics is then characterized by a complex distribution of energy among the different waves, in contrast with the 45° case where the dynamics is mostly governed by the intermediate modes.

Examination of the dissipations shows no difference between the 45° and the 80° cases for what concerns D_{plane} , while D_z is in the mean larger by a factor 2 and displays stronger fluctuations for propagation at 80° . The presence of ion-cyclotron waves for quasi-transverse propagation without a major influence on the dissipation D_z (which is indeed comparable to that observed at 45° where such modes are absent) suggests that they are not able to cascade efficiently to the dissipation scales.

5. Beyond the Hall-MHD description

Although significantly richer than classical MHD, HMHD cannot capture important dynamical properties of space plasmas originating from their quasi-collisionless character. Although such media should require a fully kinetic description and thus enormous computational resources, it may be of interest to deal with fluid models that extend MHD by retaining main kinetic effects such as Landau damping and also finite Larmor radius (FLR) corrections that, as stressed for example in Servidio et al. (2007), are expected to be comparable to the Hall effect within the magnetopause. In spite of their semi-phenomenological nature, these so-called Landau fluid models correctly reproduce the kinetic theory in the low-frequency limit.

First introduced in the context of large-scale MHD (Snyder et al., 1997), these models were then extended by retaining Hall effect and FLR corrections in order to describe quasi-transverse ionic scales obeying the gyrokinetic scaling and thus associated with low frequencies. Nevertheless, in contrast with the gyrokinetic theory, the fast magnetosonic modes are not averaged out in the Landau fluid approach and their large-scale dynamics is accurately reproduced. A comprehensive derivation of the model is given in Passot and Sulem (2007), and its reduction to one space dimension can be found in Borgogno et al. (2007).

Preliminary simulations of the Landau fluid model, retaining Landau damping of the ions and the electrons, together with ion finite Larmor radius corrections, were performed in a domain of extension 16π for a propagation angle of 80° . The Landau damping being relatively weak in quasi-transverse directions, we resorted to add a magnetic diffusivity ($\eta = 0.02$) together with a k^8 -hyperviscosity

$\nu_h = 10^{-8}$ in a simulation with a resolution of 256 collocation points. The system is driven by a random forcing acting on the transverse components of the velocity field, identical to that used in the HMHD simulation presented in section 4.2. Nevertheless, in order to control the growth of the total energy that is dominated by the global heating of the plasma, the forcing is monitored in order to maintain the kinetic energy between prescribed upper and lower bounds.

As in the HMHD corresponding simulation, we observe the development of pressure-balanced structures with the formation of small-scale fluctuations associated with whistler modes. Compressible modes are nevertheless more damped than in HMHD simulations due to Landau damping. An interesting issue that the Landau fluid can address concerns the evolution of the plasma temperatures. Figure 16 displays the typical evolution of the ion temperatures of a plasma with ion parallel beta $\beta_{\parallel i}$ equal to 0.6 (left) and 1.2 (right). We observe in both simulations that the anisotropy progressively grows up, leading to dominant transverse ion temperatures, making the plasma potentially unstable to ion mirror instabilities. For the electrons, the parallel temperature (not shown) increases, possibly leading to an electron firehose instability. Later on, we observe abrupt variations of parallel ion temperatures, resulting in a reduction of the anisotropy. These events are associated with the formation of quasi-singular structures on the velocity components, that can be shown to affect more the parallel than the perpendicular temperature. The above temperature variations was checked to be due to mirror instabilities, that is saturated thanks to the small-scale FLR corrections retained by the model. Differently, a phenomenological relaxation of temperature instabilities, in the form of effective collisions, was implemented in Sharma et al. (2006). Such a model should be useful in situations where ion-cyclotron or oblique firehose instabilities are excited, as these instabilities cannot be described with fluid equations.

The Landau fluid simulations thus reproduce constraining effects due to temperature anisotropy instabilities on the plasma parameters, also observed on solar wind data (Hellinger et al., 2006). As the plasma anisotropy relaxes under the effects of temperature instabilities, the system enters a phase of slow dynamics. This regime is however not expected to persist, as new temperature anisotropy can develop, making the above scenario to repeat.

6. Conclusion

Although limited to one space dimension, the present study reveals specific aspects of the turbulent dynamics of magnetized plasmas at scales comparable to the ion inertial length, in a regime where the transverse components of the velocity or the magnetic fields are randomly driven. Special attention was paid to the distribution of the energy among the different MHD waves that can be clearly identified from their linear dispersion relation, in spite of a

possible small shift in the temporal spectrum of the computed fields, in situations where the presence of large-scale coherent structures can be viewed as performing a renormalization of the ambient parameters.

A main observation in the case of parallel propagation is the contrast between a large-scale forcing for which the energy is almost entirely transferred to magnetosonic modes with nevertheless a non-negligible transfer to larger scales, and the regime where the driving takes place at scales where dispersion is more efficient, for which, provided the driving is of kinetic type, a direct Alfvénic transfer establishes, a result qualitatively consistent with the weak-turbulence analysis performed by Yoon and Fang (2008) in the context of the Vlasov equation. In oblique directions, the combined role of dispersion and compressibility leads to a turbulence dominated by the intermediate modes, with an increasing contribution of low frequency kinetic Alfvén waves, together with a faster establishment of total pressure balance, as the propagation angle is increased. Furthermore, the Landau fluid model shades a light on the development of pressure anisotropy resulting in recurrent instabilities.

To conclude, we would like to stress the complexity of the turbulence problem in magnetized plasmas, even within the strongly simplified description provided by one-dimensional HMHD. The usual picture of inertial ranges where energy “cascades” progressively from scale to scale at a constant rate turns out to be strongly affected by the predominance of structures and by a strongly fluctuating transfer, making possibly questionable the usual concepts of the classical turbulence theory, and leading to a dynamics that turns out to be significantly less universal.

Acknowledgments

The work was supported by “Programme National Terre Soleil” of INSU-CNRS.

- Alexandrova, O., Carbone, V., Veltri, P., Sorriso-Valvo, L., 2007. Solar wind cluster observations: turbulence spectrum and role of hall effect. *Planetary Space Sci.* 55, 2224–227.
- Alexandrova, O., Mangeney, A., Maksimovic, M., Cornilleau-Wehrin, N., Bosqued, J. M., André, M., 2006. Alfvén vortex filaments observed in magnetosheath downstream of a quasi-perpendicular bow shock. *J. Geophys. Res.* 111, A12208.
- Borgogno, D., Passot, T., Sulem, P.-L., 2007. Magnetic holes in plasmas close to mirror instability. *Nonlin. Process. Geophys.* 14, 373–383.
- Cohen, R. H., Kulsrud, R. M., 1974. Nonlinear evolution of parallel-propagating hydromagnetic waves. *Phys. Fluids* 17, 2215–2225.
- Dmitruk, Matthaeus, W. H., 2009. Waves and turbulence in magnetohydrodynamic direct numerical simulations. *Phys. Plasmas* 16, 062304.
- Galtier, S., 2006. Wave turbulence in incompressible hall magnetohydrodynamics. *J. Plasma Phys.* 72, 721–769.
- Galtier, S., Buchlin, E., 2007. Multi-scale hall-mhd turbulence in the solar win. *Astrophys. J.* 656, 560–566.
- Ghosh, S., Golstein, M. L., 1997. Anisotropy in hall mhd turbulence due to a mean magnetic field. *J. Plasma Phys.* 57, 129–154.
- Ghosh, S., Siregarand, E., Roberts, D. Q., Goldstein, M. L., 1996. Simulation of high-frequency solar wind power spectra using hall magnetohydrodynamics. *J. Geophys. Res.* 101(A2), 24932504.

- Golstein, M. L., Roberts, A., 1999. Magnetohydrodynamic turbulence in the solar wind. *Phys. Plasmas* 6, 4154.
- Gómez, D., Mahajan, S., Dmitruk, P., 2008. Hall magnetohydrodynamics in a strong magnetic field. *Phys. Plasmas* 15, 102303.
- Hellinger, P., Travnicek, P., Kasper, J. C., Lazarus, A. J., 2006. Solar wind proton temperature anisotropy: Linear theory and WIND/SWE observations. *Geophys. Res. Lett.* 33, L09101.
- Howes, G. G., 2009. Limitations of hall mhd as a model for turbulence in weakly collisional plasmas. *Nonlin. Processes Geophys.* 16, 219–232.
- Howes, G. G., Cowley, S. C., Dorland, W., Hammett, G. W., Quataert, E., Schekochihin, A. A., 2008a. A model of turbulence in magnetized plasmas: implications for the dissipation range in the solar wind. *J. Geophys. Res.* 113, A05103.
- Howes, G. G., Dorland, W., Cowley, S. C., Hammett, G. W., Quataert, E., Schekochihin, A. A., Tatsuno, T., 2008b. Kinetic simulations of magnetized turbulence in astrophysical plasmas. *Phys. Rev. Lett.* 100, 065004.
- Howes, G. G., S. C. Cowley, W. D., Hammett, G. W., Quataert, E., Schekochihin, A., 2006. Astrophysical gyrokinetics: Basic equations and linear theory. *Astrophys. J.* 651, 590–614.
- Krauss-Varban, D., Omid, N., Quest, K., 1994. Mode properties of low-frequency waves: kinetic theory versus hall-mhd. *J. Geophys. Res.* 99(A4), 5987–6009.
- Laveder, D., Borgogno, D., Passot, T., Sulem, P. L., 2009. On the efficiency of semi-implicit schemes for dispersive magnetohydrodynamics. *Computer Phys. Commun.* 180, 1860–1869.
- Leamon, R. J., Smith, C. W., Ness, N. F., Matthaeus, W. H., Wong, H. K., 1998. Observational constraints on the dynamics of the interplanetary magnetic field dissipation range. *J. Geophys. Res.* 103(A3), 4775–4787.
- Matthaeus, W. H., Servidio, S., Dmitruk, P., 2008. Comment on kinetic simulations of magnetized turbulence in astrophysical plasmas. *Phys. Rev. Lett.* 101, 149501.
- Oughton, S., Matthaeus, W. H., 2005. Parallel and perpendicular cascades in solar wind turbulence. *Nonlin. Processes Geophys.* 12, 299–310.
- Passot, T., Sulem, P. L., 2007. Collisionless magnetohydrodynamics with gyrokinetic effects. *Phys. Plasmas* 14, 082502.
- Sahraoui, F., Goldstein, M. L., Robert, P., Khotyaintsev, Y. V., 2009. Evidence of a cascade and dissipation of solar-wind turbulence at the electron gyroscale. *Phys. Rev. Lett.* 102, 231102.
- Schekochihin, A. A., Cowley, S. C., Dorland, W., Hammett, G. W., Howes, G. G., Quataert, E., Tatsuno, T., 2009. Astrophysical gyrokinetics: kinetic and fluid turbulent cascades in magnetized weakly collisional plasmas. *Astrophys. J. Suppl. Series* 182, 310–377.
- Servidio, S., Carbone, V., Primavera, L., Veltri, P., Stasiewicz, K., 2007. Compressible turbulence in hall magnetohydrodynamics. *Planetary Space Sci.* 55, 2239–2243.
- Servidio, S., Matthaeus, W. H., Carbone, V., 2008. Statistical properties of ideal three-dimensional hall magnetohydrodynamics: The spectral structure of the equilibrium ensemble. *Phys. Plasmas* 15, 042314.
- Shaikh, D., Shukla, P. K., 2009. Spectral properties of electromagnetic turbulence in plasmas. *Nonlin. Processes Geophys.* 16, 189–196.
- Sharma, P., Hammett, G. W., Quataert, E., Stone, J. M., 2006. Shearing box simulations of the mri in a collisionless plasma. *Astrophys. J.* 637, 952–967.
- Snyder, P., Hammett, G. W., Dorland, W., 1997. Landau fluid models for collisionless magnetohydrodynamics. *Phys. Plasmas* 4, 3974–3985.
- Stasiewicz, K., Shukla, P. K., Gustafsson, G., Buchert, S., Lavraud, B., Thid, B., Klos, Z., 2003. Slow magnetosonic solitons detected by the cluster spacecraft. *Phys. Rev. Lett.* 90, 085002.
- Williamson, J. H., 1980. Low-storage runge-kutta schemes. *J. Comp. Phys.* 35, 48–56.
- Yoon, P. H., Fang, T. M., 2008. Parallel cascade of Alfvén waves. *Plasma Phys. Control. Fusion* 50, 085007.
- Zank, G. P., Matthaeus, W. H., 1992. The equations of reduced magnetohydrodynamics. *J. Plasma Phys.* 48, 85.

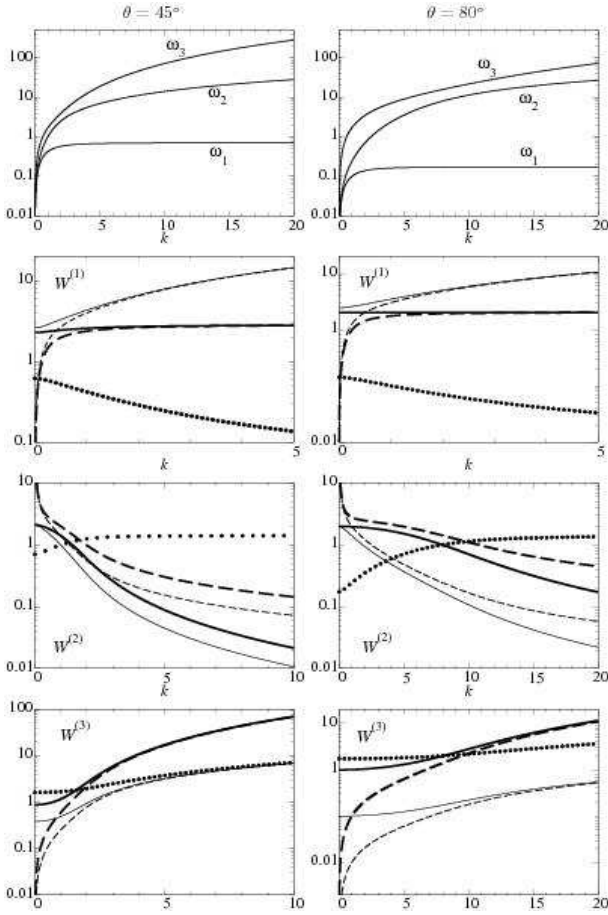


Figure 1: Wavenumber dependency of the linear HMHD eigenfrequencies (top) and eigenmode components $\mathbf{W}^{(1)}$, $\mathbf{W}^{(2)}$, $\mathbf{W}^{(3)}$ (from middle to bottom), when prescribing $\rho = 1$, for propagation angles $\theta = 45^\circ$ (left) and $\theta = 80^\circ$ (right): magnetic field b_y (thick solid line) and b_z (thick dashed line); velocity components v_y (thin solid line) and v_z (thin dashed line); velocity component v_x (dotted line).

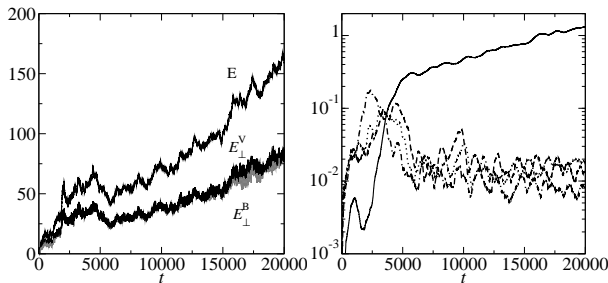


Figure 2: Left: time evolution of the total energy and of the transverse kinetic and magnetic contributions for run A with kinetic forcing discussed in Section 3.1. Right: time evolution of the magnetic energy $|\hat{\mathbf{b}}_y|^2 + |\hat{\mathbf{b}}_z|^2$ for the Fourier modes of index 1 (solid line), 2 (dashed), 3 (dotted), 4 (dash-dotted), for the same simulation.

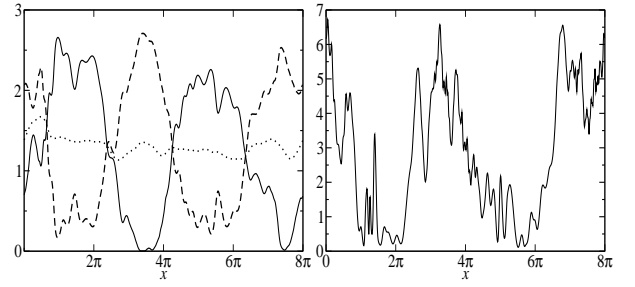


Figure 3: Left: profile of the the magnetic pressure $|\mathbf{b}_\perp|^2/2$ (solid line) and of the thermal pressure $\beta\rho^\gamma/\gamma$ (dashed line), together with their half-sum (dotted line) showing pressure balance at time $t = 20000$ for the run A. Right: transverse velocity field intensity $|\mathbf{v}_\perp|^2$ at the same time.

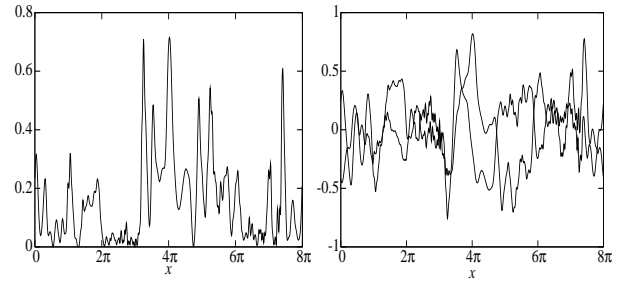


Figure 4: Transverse velocity field intensity ($|\mathbf{v}_\perp|^2$) (left) and individual components v_y , v_z at time $t = 18200$ for run A, after filtering the mode of index $n = 1$.

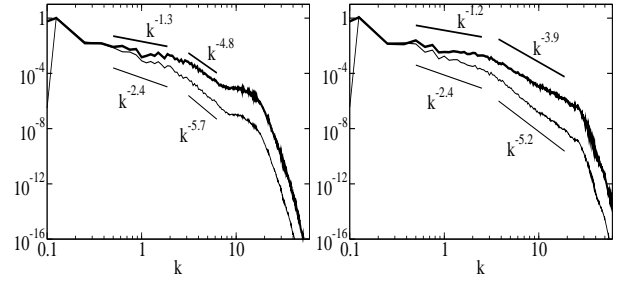


Figure 5: Kinetic $|\hat{\mathbf{v}}_y|^2 + |\hat{\mathbf{v}}_z|^2$ (thick line) and magnetic $|\hat{\mathbf{b}}_y|^2 + |\hat{\mathbf{b}}_z|^2$ (thin line) spectra averaged over the time interval $t = 18200 - 18250$ (left), and $t = 19500 - 19550$ (right) for run A.

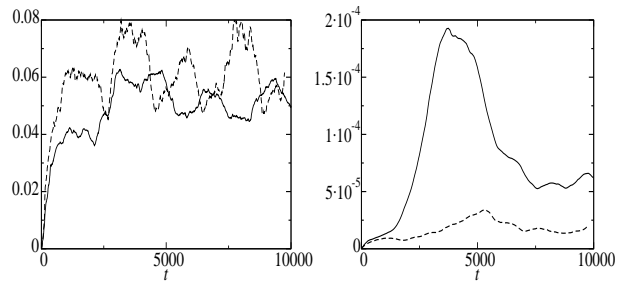


Figure 6: Left: time evolution of the parallel dissipation D_\parallel for the kinetic (solid line) and magnetic (dashed line) drivings (runs A and B respectively) described in Section 3.1. Right: same for the perpendicular dissipation D_\perp .

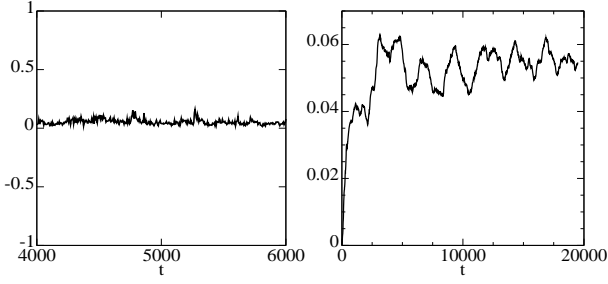


Figure 7: Time evolution of the parallel dissipation (dark line) and of the rate of energy transfer S from the Alfvén to magnetosonic waves (light line) for run A. Left: instantaneous quantities. Right: time-averaged quantities over $\Delta t_{\text{ave}} = 1000$.

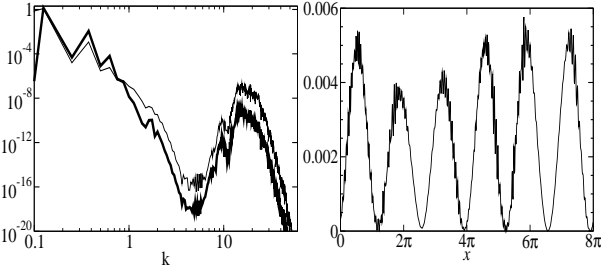


Figure 8: Left: kinetic $|\hat{\mathbf{v}}_y|^2 + |\hat{\mathbf{v}}_z|^2$ (thick line) and magnetic $|\hat{\mathbf{b}}_y|^2 + |\hat{\mathbf{b}}_z|^2$ (thin line) spectra averaged over the time interval $t = 28000 - 28050$ for the kinetically driven run of Section 3.1 with monitored forcing. Right: transverse velocity field intensity ($|\mathbf{v}_\perp|^2$) at time $t = 28000$, in the same conditions.

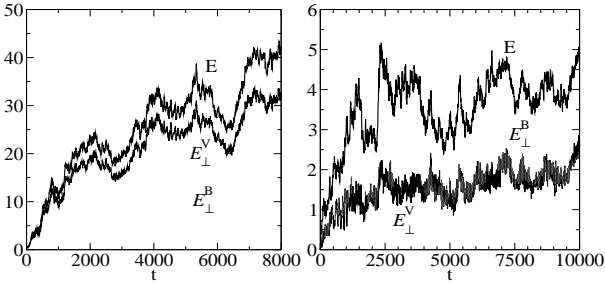


Figure 10: Time evolution of the total kinetic and magnetic energies for kinetic (left) or magnetic (right) drivings (runs C and D respectively) in the conditions described in Section 3.2.

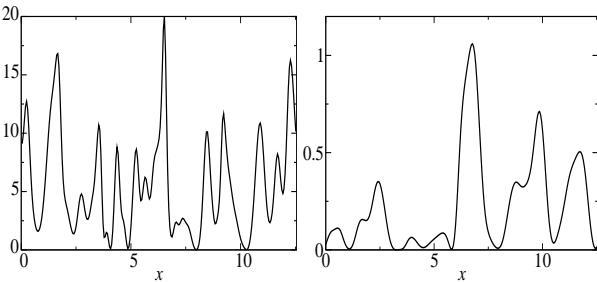


Figure 11: Profile of $|\mathbf{v}_\perp|^2$ at $t = 4000$ for kinetic (run C, left) and magnetic (run D, right) driving for the run described in Section 3.2.

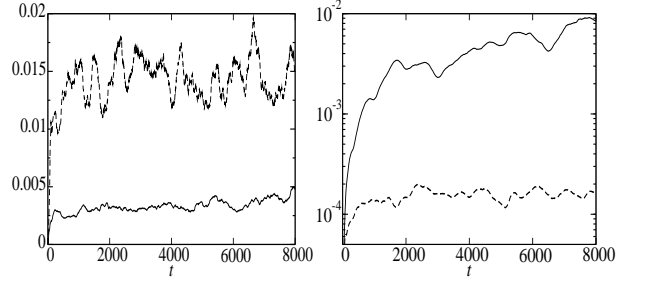


Figure 12: Left: time evolution of the parallel dissipation D_\parallel for the kinetic (run C, solid line) and magnetic (run D, dashed line) drivings in the conditions described in Section 3.2. Right: same for the perpendicular dissipation D_\perp (in lin-log scale).

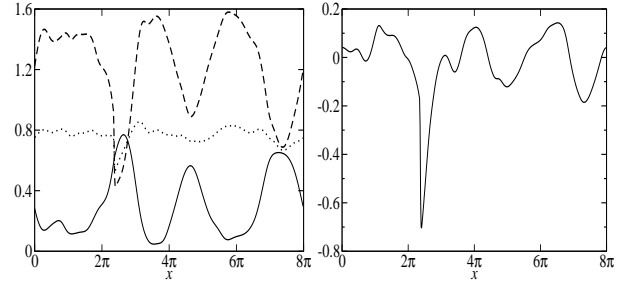


Figure 13: Left: profile of the the magnetic $|\mathbf{b}_\perp|^2/2$ (solid line) and thermal $\beta\rho\gamma/\gamma$ (dashed line) pressures, together with their half-sum (dotted line) at time $t = 422$, for the run E with large-scale kinetic driving described in Section 4.1. Right: velocity component v_x at the same time.

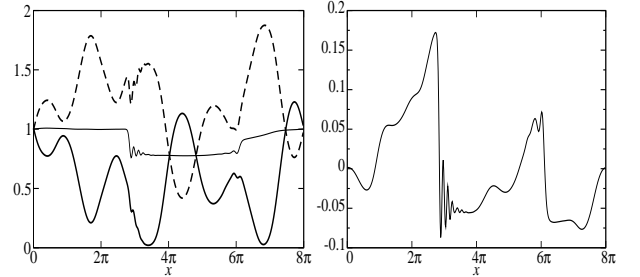


Figure 14: Left: profile of the the magnetic $|\mathbf{b}_\perp|^2/2$ (solid line) and thermal $\beta\rho\gamma/\gamma$ (dashed line) pressures, together with their half-sum (dotted line) at time $t = 2472$ for run H with large-scale kinetic driving described in Section 4.2. Right: velocity component v_x at the same time.

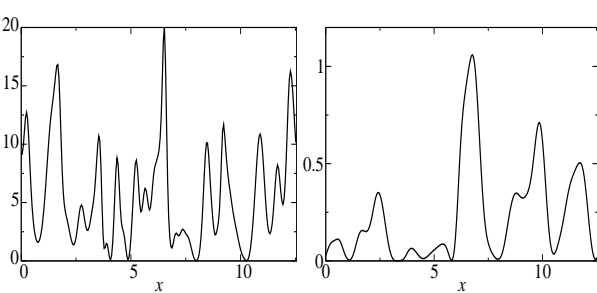


Figure 15: Spectra $|\hat{\mathbf{v}}_\perp|^2$ (thick line) and $|\hat{\mathbf{b}}_\perp|^2$ (thin line) of the transverse fields, averaged over the time intervals $t = 2465 - 2477$ (left), and $t = 10595 - 10565$ (right) for run H.

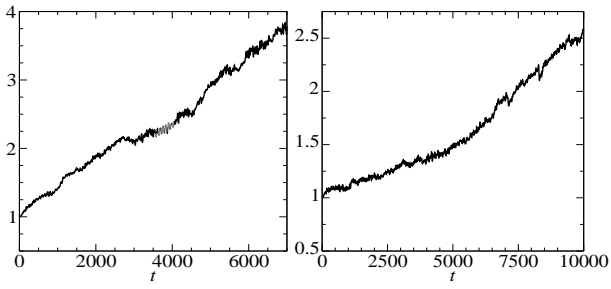


Figure 16: Time evolution of the parallel (grey line) and transverse (black line) temperatures for simulations with $\beta_{\parallel i} = 0.6$ (left) and $\beta_{\parallel i} = 1.2$ (right) for the runs described in Section 5.